J. Fluid Mech. (2004), *vol.* 510, *pp.* 333–352.
DOI: 10.1017/S0022112004009589 Printed in the United Kingdom

Bounds on dissipation in stress-driven flow

By W. TANG[1], C. P. CAULFIELD[1] AND W. R. YOUNG[2]

[1]Department of Mechanical and Aerospace Engineering, Jacobs School of Engineering, University of California, San Diego, 9500 Gilman Drive, La Jolla, CA 92093-0411, USA

[2]Scripps Instititution of Oceanography, University of California, San Diego, 9500 Gilman Drive, La Jolla, CA 92093-0213, USA

(Received 22 December 2003 and in revised form 15 March 2004)

We calculate the optimal upper and lower bounds, subject to the assumption of streamwise invariance, on the long-time-averaged mechanical energy dissipation rate ε within the flow of an incompressible viscous fluid of constant kinematic viscosity ν and depth h driven by a constant surface stress $\tau = \rho u_\star^2$, where $u_\star$ is the friction velocity. We show that $\varepsilon \leqslant \varepsilon_{\max} = \tau^2/(\rho^2\nu)$, i.e. the dissipation is bounded above by the dissipation associated with the laminar solution $\boldsymbol{u} = \tau(z+h)/(\rho\nu)\hat{\boldsymbol{\imath}}$, where $\hat{\boldsymbol{\imath}}$ is the unit vector in the streamwise x-direction.

By using the variational 'background method' (due to Constantin, Doering and Hopf) and numerical continuation, we also generate a rigorous lower bound on the dissipation for arbitrary Grashof numbers G, where $G = \tau h^2/(\rho\nu^2)$. Under the assumption of streamwise invariance as $G \to \infty$, for flows where horizontal mean momentum balance and total power balance are imposed as constraints, we show numerically that the best possible lower bound for the dissipation is $\varepsilon \geqslant \varepsilon_{\min} = 7.531u_\star^3/h$, a bound that is independent of the flow viscosity. This scaling (though not the best possible numerical coefficient) can also be obtained directly by applying the same imposed constraints and restricting attention to a particular, analytically tractable, class of mean flows.

1. Introduction

Forced turbulent flows occur in a wide range of natural and industrial fluid flows. Identifying scaling laws for the mechanical energy dissipation rate within such flows has been widely studied, in an effort to capture how the turbulent small-scale motions dissipate the energy input by the forcing. Naturally, the properties of the mechanical energy dissipation rate are strongly dependent on the characteristics of the forcing of the flow. One particular type of forcing that commonly occurs is the application of stress at the upper surface of a layer of fluid over a solid lower surface as happens, for example, when wind blows over a body of water. It is reasonable to suppose that this injection of energy at the upper surface will determine both the bulk and small-scale properties of the flow in the forced fluid layer, with the no-slip lower surface boundary condition also playing a critically important role. In this paper we address the fundamental question of how the forcing affects the flow by determining both upper and lower bounds on the mechanical energy dissipation rate for flows that are statistically stationary, thus defining a range of possible behaviours of such a flow.

We concentrate on generating bounds for the mechanical energy dissipation rate, as such bounds can be derived rigorously without introducing heuristic modelling

assumptions or approximations. In this paper, we use the variational method developed by Constantin and Doering utilizing a mathematical device introduced by Hopf (1941) (Doering & Constantin 1992, 1994; Constantin & Doering 1995; Doering & Constantin 1996; Nicodemus, Grossmann & Holthaus 1997*a*, *b*, 1998*a*, *b*) to construct a bound on the mechanical energy dissipation rate. Following Plasting & Kerswell (2003, henceforth referred to as PK03), we refer to this method as the CDH method. The CDH method uses a non-unique decomposition of the velocity distribution into a steady 'background' that satisfies the inhomogeneous boundary conditions, and 'fluctuations' away from this background satisfying homogeneous boundary conditions. It is important to stress that the background does not necessarily correspond to the horizontal average of the flow. Such decompositions can then be used to construct rigorous bounds on flow quantities of interest, consistently with imposed dynamic and kinematic constraints, using conventional techniques of the calculus of variations. Kerswell (1997, 1998, 2001) demonstrated that this method produces the complementary variational problem to the earlier approach pioneered by Howard (1963, 1972, 1990) and Busse (1969*a*, *b*, 1970, 1978), developing ideas originally proposed by Malkus (1954, 1956).

With the added, reasonable (though unproven) assumption that flows associated with the bounds do not have any streamwise variation (Busse 1969*a*, 1970; Nicodemus *et al.* 1998*a*) PK03 demonstrated that numerical continuation methods (using the continuation program PITCON of Rheinbolt & Burkardt 1983*a*, *b*) can be used to generate optimal solutions to the full Euler–Lagrange equations arising from the simple dynamical constraints of total power balance, and horizontally averaged streamwise momentum balance. They considered the canonical problem of generating an upper bound on the mechanical energy dissipation rate in plane Couette flow, identifying the best possible upper bound numerically. (Of course, Couette flow is qualitatively different from stress-driven flow, as Couette flow fixes the boundary velocity, not the boundary velocity gradient.) Since Couette flow geometry had been previously widely considered, (e.g. Busse 1970; Nicodemus *et al.* 1998*a*) they were able to identify the extent to which the full numerical solution improved the bound compared to studies that considered somewhat more restrictive classes of trial functions, and also to identify the important qualitative characteristics of the flows associated with the bounding solutions.

Several studies of forced flows have considered both periodic domains (Childress, Kerswell & Gilbert 2001; Doering & Foias 2002) and flows with stress-free boundary conditions (Doering, Eckhardt & Schumacher 2003). However, there has been no previous study of the particular flow geometry of interest here, although Otero *et al.* (2002) did consider the somewhat analogous problem of Rayleigh–Bénard convection with an imposed heat flux. Their analysis did not solve a full variational problem, but rather restricted attention to piecewise linear profiles in the temperature field. Therefore, we are not only interested in generating the best possible bound using numerical continuation methods, but also in considering more restrictive classes of smooth trial functions that nevertheless enable us to capture the dominant scaling of the mechanical energy dissipation rate.

Towards these ends, the rest of the paper is organized as follows. In § 2, we define appropriately the stress-driven flow model, and also prove that, for a given surface stress, laminar flow yields the largest possible mechanical energy dissipation rate. In § 3, we generate a lower bound on the mechanical energy dissipation rate. We first construct a simple lower bound using a special family of trial functions for the long-time average of the flow. These simple trial functions capture the dominant scaling

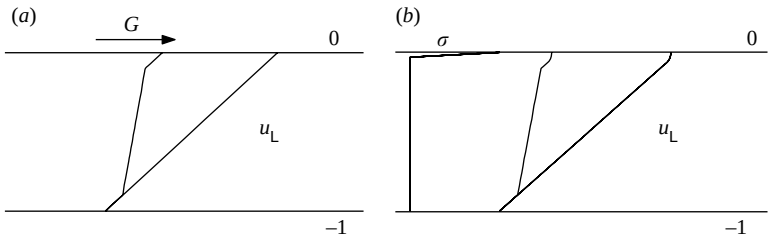

FIGURE 1. Schematic diagrams comparing (*a*) the surface-stress-driven flow A; (*b*) the body-forced flow B.

of the flow associated with a lower bound on the mechanical energy dissipation rate, and they prove very useful in developing an understanding of the significant physical processes, since the effect of the constraints of total power balance and streamwise momentum balance can be identified explicitly.

However, as we show in § 4, this simple bound leads to a quantitative underestimate of the magnitude of the the best possible lower bound on the mechanical energy dissipation rate consistent with the imposed constraints of streamwise independence, total power balance, and streamwise mean momentum balance. To establish this fact, and to identify the actual numerical value of the best possible bound in a straightforward manner, we first show the equivalence of the upper surface stress-driven flow to a body-forced flow model with a stress-free upper surface boundary condition, which is much more straightforward to consider within the CDH framework. We then solve the full CDH problem to achieve the rigorous lower bound, using a numerical method similar to the one discussed in PK03, and present our results for the bounds and the associated flow structures. We discuss the properties of our findings, comparing the results of the two distinct calculations, paying particular attention to the extent to which the restrictive trial functions discussed in § 3 manage to capture properties of the general flow calculated in § 4. Finally, in § 5, we draw some conclusions, and suggest some future work, in particular the direct numerical simulation of the flow to investigate how closely real flows approach the calculated bounds.

2. Formulation

We consider an incompressible layer of fluid of constant depth h, density ρ and kinematic viscosity ν. We impose long-time-average and both x-periodic and y-periodic boundary conditions across $-L_x < x < L_x$, and $-L_y < y < L_y$ and so introduce a time and horizontal averaging operator:

$$\overline{q(\boldsymbol{x},t)} \equiv \lim_{T\to\infty} \frac{1}{4L_yL_xT} \int_0^T \int_{-L_y}^{L_y} \int_{-L_x}^{L_x} q(\boldsymbol{x},t)\,\mathrm{d}x\,\mathrm{d}y\,\mathrm{d}t, \tag{2.1}$$

and a volume average:

$$\langle q(\boldsymbol{x},t)\rangle = \int_{-h}^{0} \bar{q}\,\mathrm{d}z. \tag{2.2}$$

In this flow, which we shall refer to subsequently as flow A, the motion is driven by surface stress $\tau = \rho u_\star^2$ applied at the upper surface, $z = 0$, where $u_\star$ is the friction velocity. It is shown schematically in figure 1(*a*). At the bottom $z = -h$, we impose a no-slip boundary condition. We non-dimensionalize the Navier–Stokes equations

using ρ, ν and h to define units of length, time and mass. The non-dimensional Navier–Stokes equations for flow A are thus

$$\boldsymbol{u}_t + \boldsymbol{u}\cdot\nabla\boldsymbol{u} + \nabla p - \nabla^2\boldsymbol{u} = 0, \tag{2.3}$$

with the incompressibility condition

$$\nabla\cdot\boldsymbol{u} = 0, \tag{2.4}$$

and boundary conditions

$$u_{1z}(0) = G,\ u_{2z}(0) = 0,\ u_3(0) = 0; \quad u_1(-1) = u_2(-1) = u_3(-1) = 0. \tag{2.5}$$

The important non-dimensional group is the Grashof number, defined as

$$G \equiv \frac{\tau h^2}{\rho\nu^2} = \frac{u_\star^2 h^2}{\nu^2}. \tag{2.6}$$

We characterize the flow using the mechanical energy dissipation per unit mass, ε:

$$\varepsilon \equiv \frac{\nu^3}{h^4}\langle\|\nabla\boldsymbol{u}\|^2\rangle, \tag{2.7}$$

where the non-dimensional deformation is

$$\|\nabla\boldsymbol{u}\|^2 \equiv |\nabla u_1|^2 + |\nabla u_2|^2 + |\nabla u_3|^2. \tag{2.8}$$

The laminar solution to equations (2.3) and (2.4) is simply the Couette flow $\boldsymbol{u}_{\mathrm{L}} = G(z+1)\hat{\boldsymbol{\imath}}$. We can now show that ε in (2.7) is bounded from above by the mechanical energy dissipation of this laminar solution,

$$\varepsilon_{\mathrm{L}} \equiv \frac{\nu^3}{h^4}G^2 = \frac{u_\star^4}{\nu}. \tag{2.9}$$

Taking the time and volume average of the dot product of $\boldsymbol{u}$ and the left-hand side of (2.3), and applying the boundary conditions, we obtain

$$\langle\|\nabla\boldsymbol{u}\|^2\rangle - G\langle\bar{u}_{1z}\rangle = 0\ (\mathscr{D}_1 = 0), \tag{2.10}$$

using the convention that $\mathscr{D}_i$ denotes a group of important terms. Using this result to eliminate the cross-terms on the left-hand side of

$$\langle|\nabla\boldsymbol{u} - \nabla\boldsymbol{u}_{\mathrm{L}}|^2\rangle \geqslant 0, \tag{2.11}$$

we obtain

$$\varepsilon_{\mathrm{L}} \geqslant \varepsilon. \tag{2.12}$$

3. A lower bound for flow A

In this section we apply relatively elementary arguments to flow A and obtain a complementary lower bound on the mechanical energy dissipation rate ε. Although the basic idea is similar to the CDH method, the procedure is simpler than that required to generate the full bound, as we show in §4. As we see, the two bounds have the same asymptotic structure and scaling for large G, although, naturally, the simpler bound is not as strong. To generate the bound, we exploit certain properties of the flow. As discussed above, (2.10) yields an expression which captures the long-time total power balance of the flow, with the dissipation being balanced by the energy injection through stress at the top surface into the mean flow shear. We can

obtain a second expression for the dissipation by writing the total flow velocity as $\boldsymbol{u} = \bar{u}_1(z)\hat{\boldsymbol{\imath}} + \boldsymbol{u}'(\boldsymbol{x}, t)$ and then using that decomposition to obtain

$$\langle \|\boldsymbol{\nabla u}\|^2 \rangle - \langle \bar{u}_{1z}^2 \rangle - \langle \|\boldsymbol{\nabla u}'\|^2 \rangle = 0 \quad (\mathscr{D}_2 = 0). \tag{3.1}$$

Finally, horizontally averaging the streamwise Navier–Stokes momentum equation (2.3) yields the constraint

$$\overline{u_1' u_3'} - \bar{u}_{1z} + G = 0 \quad (\mathscr{D}_3 = 0). \tag{3.2}$$

This important momentum flux constraint shows that the applied stress at the top surface is transmitted downwards by the Reynolds' correlation, $\overline{u_1' u_3'}$, and ultimately balanced by a viscous bottom stress. We now use the three results (2.10), (3.1), and (3.2) above to obtain a lower bound on $\langle \|\boldsymbol{\nabla u}\|^2 \rangle$.

3.1. *Constructing the simple bound*

Assuming that $\theta(z)$ is an arbitrary function of z, we combine the left-hand sides $\mathscr{D}_1$, $\mathscr{D}_2$ and $\mathscr{D}_3$ of (2.10), (3.1) and (3.2) respectively to obtain the expression

$$\mathscr{D}_2 + \alpha \mathscr{D}_1 + G \int_{-1}^{0} \theta(z) \mathscr{D}_3 \, \mathrm{d}z = 0, \tag{3.3}$$

where α is an adjustable parameter which we will select to obtain the best possible bound for given choices of $\theta(z)$. (Although $\theta(z)$ bears some resemblance to the multiplier functions used in Doering *et al.* (2003), there are no boundary conditions required, as the role of $\theta(z)$ is merely to impose the horizontally averaged streamwise momentum constraint $\mathscr{D}_3 = 0$, as defined in (3.2), at all heights in the flow domain.) This expression may be thought of as a combination of a definition for the dissipation ε in terms of a decomposition into mean and perturbation velocity components and two constraints which impose total power balance and streamwise mean momentum balance. These two constraints – as well as the implicit imposition of the incompressibility condition (2.4) – are the only ones imposed on $\boldsymbol{u}$, and in particular, it is vital to appreciate that we do not require $\boldsymbol{u}$ to be a solution of the Navier–Stokes equations (2.3). Of course, any solution of the Navier–Stokes equations does indeed satisfy these constraints, and so a bound constructed for this broader class of functions $\boldsymbol{u}$ is also a bound for the incompressible velocity solutions to the Navier–Stokes equations.

Completing a square in (3.3) we find that

$$(1+\alpha)\langle \|\boldsymbol{\nabla u}\|^2 \rangle = G^2 \langle \theta \rangle - \tfrac{1}{4} G^2 \langle (\alpha - \theta)^2 \rangle + \left\langle \left[\bar{u}_{1z} + \tfrac{1}{2} G(\alpha - \theta) \right]^2 \right\rangle + \mathscr{J}[\boldsymbol{u}'; \theta], \tag{3.4}$$

where

$$\mathscr{J}[\boldsymbol{u}'; \theta] \equiv \langle \|\boldsymbol{\nabla u}'\|^2 \rangle + G \langle \theta u_1' u_3' \rangle. \tag{3.5}$$

Analogously to the approach of the CDH method, a necessary condition for (3.4) to generate a lower bound on the dissipation is the functional constraint that

$$\mathscr{J}[\boldsymbol{v}; \theta] \geqslant 0, \tag{3.6}$$

for all incompressible vector fields $\boldsymbol{v}$ which satisfy the same boundary conditions as $\boldsymbol{u}'$. This is a constraint on the allowable functions $\theta(z)$, which leads to a variational problem discussed in the Appendix. Such constraints are commonly referred to as 'spectral constraints' within the framework of the CDH method, although unlike in the CDH method, we impose no boundary conditions on $\theta(z)$, just that $\mathscr{J} \geqslant 0$.

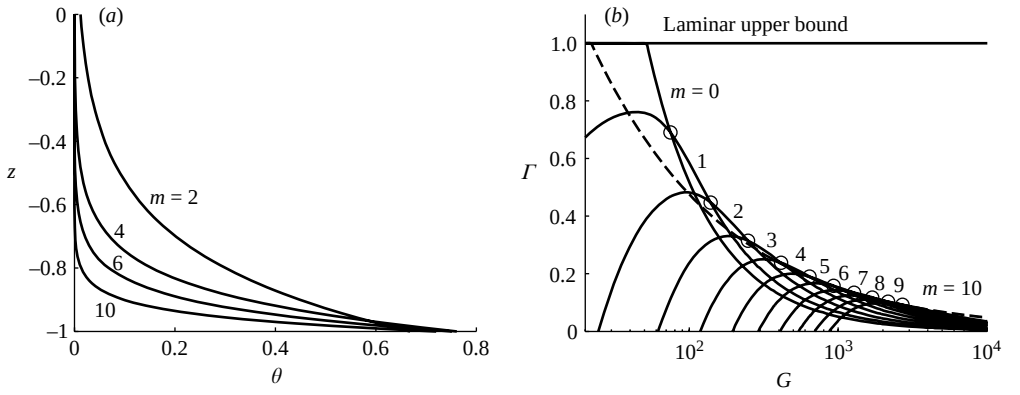

FIGURE 2. (*a*) The variation with z of the exponential class of functions $\theta(z)$ as defined in (3.10) for: $m = 2$, 4, 6 and 10. In each case, we have plotted $\theta(z)$ at the value of G corresponding to the smallest value at which $\theta(z)$ with the given value of m leads to the best lower bound on the mechanical energy dissipation rate. (*b*) Γ (as defined in (3.7)) against G for various members of the family of functions $\theta(z)$ as defined in (3.10), each curve being labelled by the associated value of the parameter m. The smallest value of G for which each $\theta(z)$ associated with a particular value of m leads to the best lower bound on the mechanical energy dissipation rate is marked with a circle. Note that $\Gamma = \varepsilon/\varepsilon_{\mathrm{L}}$ must lie above every curve. The best lower bound on Γ for this family is thus given by the envelope of these curves. The asymptotic value of Γ for large G defined by (3.15) is shown with a dashed line.

Requiring (3.6) and $1 + \alpha > 0$, we can obtain a lower bound on ε by dropping the final two non-negative terms on the right-hand side of (3.4) to obtain

$$\Gamma \equiv \varepsilon/\varepsilon_{\mathrm{L}} = G^{-2}\langle \|\boldsymbol{\nabla u}\|^2 \rangle \geqslant \frac{\langle\theta\rangle}{1+\alpha} - \frac{\langle(\alpha-\theta)^2\rangle}{4(1+\alpha)}. \tag{3.7}$$

This bound (3.7) is optimized, for a given choice (or class of choices) of θ, by maximizing the right-hand side as a function of α. The optimal value of α is

$$1 + \alpha = \sqrt{\langle(1-\theta)^2\rangle}, \tag{3.8}$$

in which case

$$\Gamma \geqslant \tfrac{1}{2}[1 + \langle\theta\rangle - \sqrt{\langle(1-\theta)^2\rangle}]. \tag{3.9}$$

We thus can investigate what the properties of this bound are for particular choices for $\theta(z)$.

3.2. *The exponential family*

As a specific example for (3.9), we consider the 'exponential' class of functions θ:

$$\theta(z) = \beta m \operatorname{cosech} m \, \mathrm{e}^{-m-2mz}. \tag{3.10}$$

Here, m is a profile parameter and the amplitude β is defined so that $\beta = \langle\theta\rangle$. The function is chosen so that if $m \gg 1$, there is a boundary layer at the bottom, with depth $O(1/m)$, decaying towards very small values in the interior and as $z \to 0$. Therefore, unsurprisingly, since θ essentially imposes the horizontally averaged streamwise momentum constraint (3.2), the bottom boundary layer viscous stress is critically important in the flow balance. Several curves for different values of m are shown in figure 2.

To ensure that that every member of this family satisfies the condition $\mathscr{I} \geqslant 0$ (as defined in (3.5)) we use the numerical solution of the eigenproblem in the Appendix to determine βG as a function of m. For the family (3.10) the bound in (3.9) is then

$$\Gamma \geqslant \tfrac{1}{2}[1 + \beta - \sqrt{1 - 2\beta + \beta^2 m \coth m}]. \tag{3.11}$$

Plotting the right-hand side of (3.11) as a function of G for several values of m we obtain the result in figure 2(*b*). The best lower bound on Γ is then obtained as the envelope generated by varying m.

If $G \gg 1$ then we can simplify (3.11) and obtain a compact expression for the lower bound. With $G \gg 1$ we see from figure 2 that the optimal m is also large. In this case the numerical solution in the Appendix gives

$$\beta G \approx 38.640 m. \tag{3.12}$$

Although m is large, $\beta^2 m$ is small and the right-hand side of (3.11) simplifies to

$$\Gamma \geqslant \beta - \tfrac{1}{4}\beta^2 m. \tag{3.13}$$

The optimal value of m is now found by using (3.12) to eliminate β from (3.13) and then maximizing the left-hand side of the inequality (3.13) with respect to m. This gives

$$\beta = \frac{2}{\sqrt{3}}\left(\frac{38.640}{G}\right)^{1/2}, \qquad m = \frac{2}{\sqrt{3}}\left(\frac{G}{38.640}\right)^{1/2}. \tag{3.14}$$

This expression implies that the boundary layer depth of the family θ defined in (3.10) is $O(G^{-1/2})$ as $G \to \infty$. With the optimal m at hand, the sharpest bound available from (3.13) is

$$\gamma \equiv \Gamma G^{1/2} = \frac{\varepsilon h}{u_\star^3} \geqslant 4.785. \tag{3.15}$$

This result is satisfying because the lower bound on the dissipation becomes independent of ν, and corresponds to an expected inertial scaling ($\varepsilon = O(u_\star^3/h)$) as $G \to \infty$. Also, although this approach does not determine all the properties of the flow associated with the bound, from the expression for total power balance (3.1)

$$\langle \bar{u}_{1z} \rangle = \bar{u}_1|_{z=0} = \bar{u}_1(0) = O\big(G^{1/2}\big). \tag{3.16}$$

Therefore, the lower bound is associated with a flow where the surface mean velocity has been decelerated (presumably by turbulent processes) from the laminar flow value $\bar{u}_1(0) = G$ to a typically substantially smaller value which is $O(G^{1/2})$. Dimensionally, this surface velocity $\bar{u}_1(0) = O(u_\star)$, independently of viscosity, which appears reasonable.

We experimented with more elaborate classes of θ than the exponential functions defined in (3.10), e.g. with boundary layers at both $z = 0$ and $z = 1$. This results in modest improvements on (3.15) by increasing the numerical coefficient to above 5. However the CDH method is more systematic, and so in the next section we construct the best possible bound subject to the same imposed constraints of total power balance (2.10) and horizontally averaged streamwise momentum balance (3.2), paying particular attention to the extent to which the simplified bound constructed above compares to this best possible bound.

4. The optimal lower bound obtained with the CDH method

For technical mathematical reasons, when using the CDH method, it is more convenient to consider a flow that is different from the flow A considered above. These technical difficulties are associated with the treatment of boundary variations (see e.g. Courant & Hilbert 1953) due to the non-vanishing stress at the top $z = 0$ of the flow domain. The flow geometry of this second flow, which we shall henceforth refer to as flow B, is the same as flow A, although the boundary conditions and forcing are different. In flow B, we assume that there is a stress-free upper boundary condition, $u_{1z}(0) = 0$. We also assume that flow B is driven by a depth-dependent body force, $G\sigma_z\hat{\boldsymbol{i}}$, where $\hat{\boldsymbol{i}}$ is the unit vector in the streamwise x-direction, and $\sigma(z)$ is a non-dimensional shape function, which is zero at $z = 0$ (to allow for the stress-free condition) and is normalized so that $\langle\sigma^2\rangle = 1$. For this flow, the governing equations are

$$\left.\begin{aligned} \boldsymbol{u}_t + \boldsymbol{u}\cdot\nabla\boldsymbol{u} + \nabla p - \nabla^2\boldsymbol{u} = G\sigma_z\hat{\boldsymbol{i}} \\ \nabla\cdot\boldsymbol{u} = 0. \end{aligned}\right\} \tag{4.1}$$

with homogeneous boundary conditions

$$u_{1z}(0) = 0,\ u_{2z}(0) = 0,\ u_3(0) = 0; \quad u_1(-1) = u_2(-1) = u_3(-1) = 0. \tag{4.2}$$

Although different, under certain circumstances, and for particular choices of the shape function σ, the behaviours of flow A and flow B can approach equivalence arbitrarily closely. This agreement can be obtained by allowing σ to vary substantially only in an arbitrarily narrow upper boundary region. Therefore, flow B, driven by a body force concentrated near $z = 0$, and shown schematically in figure 1(*b*), can be used as a model for the surface-stress-driven flow A discussed above. Flow B is mathematically convenient within the context of a variational problem, due to the technical difficulties mentioned above associated with the fixed-stress upper boundary condition of flow A. An example of the possibility for close correspondence can be identified by recalling that for flow A, the laminar state solution is $u_{\mathrm{L}z} = G$, a Couette profile. For flow B we can simply choose $\sigma \approx -1$ over all but a thin surface layer, where $\sigma_z \neq 0$ as σ changes from -1 to 0 at the boundary. The laminar solution for flow B, $u_{\mathrm{L}z} = -G\sigma\hat{\boldsymbol{i}}$, then closely approximates the laminar solution to flow A.

In this section we apply the CDH method to find a lower bound on the dissipation ε in terms of G and the structure of the shape function $\sigma(z)$. Following the conventional methodology for flow B, we consider a non-unique decomposition of the velocity field $\boldsymbol{u} = (u_1, u_2, u_3)$ into a steady one-dimensional 'background' $\phi(z)\hat{\boldsymbol{i}}$ that agrees with the actual fluid velocity $\boldsymbol{u}$ at the boundaries and a three-dimensional, unsteady 'fluctuation' $\boldsymbol{v}(\boldsymbol{x}, t) = (v_1, v_2, v_3)$ with homogeneous boundary conditions, i.e.

$$\boldsymbol{u}(\boldsymbol{x}, t) = \phi(z)\hat{\boldsymbol{i}} + \boldsymbol{v}(\boldsymbol{x}, t), \tag{4.3}$$

where

$$\boldsymbol{v} = \phi = 0 \quad \text{at } z = -1, \quad \phi_z = v_{1z} = v_{2z} = v_3 = 0 \text{ at } z = 0. \tag{4.4}$$

It is important to appreciate that this decomposition is non-unique, and that the background field ϕ does not necessarily correspond to horizontal spatial averages of the total flow fields since horizontal averages of the so-called 'fluctuation' field $\bar{\boldsymbol{v}}$ may be non-zero. It is also convenient to separate the fluctation velocity $\boldsymbol{v}$ into a mean part $\bar{v}_1(z)\hat{\boldsymbol{x}}$ and a meanless part $\hat{\boldsymbol{v}}(\boldsymbol{x}, t)$:

$$\boldsymbol{v}(\boldsymbol{x}, t) = \bar{v}_1(z, t)\hat{\boldsymbol{i}} + \hat{\boldsymbol{v}}(\boldsymbol{x}, t), \qquad \overline{\hat{\boldsymbol{v}}} = 0. \tag{4.5}$$

We consider the Lagrangian functional $\mathscr{L}$:

$$\mathscr{L} = \lim_{t\to\infty} \frac{1}{t} \int_0^t [\langle \|\nabla \boldsymbol{u}\|^2 \rangle + a\langle \boldsymbol{v}\cdot(\boldsymbol{u}_t + \boldsymbol{u}\cdot\nabla\boldsymbol{u} + \nabla p - \nabla^2\boldsymbol{u} - G\sigma_z\hat{\boldsymbol{\imath}})\rangle] \,\mathrm{d}t. \tag{4.6}$$

In this expression, $a\boldsymbol{v}$ is a Lagrange multiplier that formally imposes the Navier–Stokes equations (4.1). However, after some manipulation, since $\boldsymbol{v} = \boldsymbol{u} - \phi\hat{\boldsymbol{\imath}}$, (4.6) is actually equivalent to

$$\mathscr{L} = \langle \|\nabla \boldsymbol{u}\|^2 \rangle + a(\langle \|\nabla \boldsymbol{u}\|^2 \rangle + G\,\langle \sigma \bar{u}_{1z}\rangle) + \langle a\phi_z\,(\overline{u_1 u_3} - \bar{u}_{1z} - G\sigma)\rangle, \tag{4.7}$$

where terms involving time derivatives have been assumed to be zero over sufficiently long time averages. Therefore, the actual constraints that are being applied are merely total power balance, and horizontally averaged streamwise momentum balance, just as in § 3. Indeed, if we choose the body forcing shape function $\sigma \approx -1$ except near the upper boundary, the constraints imposed in (4.7) approach arbitrarily close to the constraints $\mathscr{D}_1 = 0$ and $\mathscr{D}_3 = 0$ imposed in (3.3), if we identify α with the Lagrange multiplier a, and $G\theta$ with the Lagrange multiplier $a\phi_z$. This expression also shows a further attraction of using the CDH method decomposition: the background ϕ acts as a Lagrange multiplier to impose the horizontally averaged streamwise momentum constraint defined in (3.2).

In this section, using the calculus of variations, we aim to find the minimum stationary value of $\mathscr{L}$ over all possible $\boldsymbol{u}$, $\boldsymbol{v}$, ϕ, and a consistent with the boundary conditions. Using the decomposition (4.5), $\mathscr{L}$ can also be written as

$$\begin{aligned}\mathscr{L}[a,\phi,\boldsymbol{v}] = \langle \phi_z^2\rangle + (2+a)\,\langle \phi_z \bar{v}_{1z}\rangle + (1+a)\,\langle \bar{v}_{1z}^2\rangle + (1+a)\langle \|\nabla\hat{\boldsymbol{v}}\|^2\rangle \\ + a\,\langle \hat{v}_1\hat{v}_3\phi_z\rangle + a\,\langle \hat{\boldsymbol{v}}\cdot\nabla p\rangle - aG\,\langle \bar{v}_1\sigma_z\rangle.\end{aligned} \tag{4.8}$$

From this expression, it is now apparent specifically why we choose to consider the body-forced flow B rather than the equivalent surface-stress-driven flow A. Modelling the surface localized stress by means of a body force that varies with depth allows the effect of the last term in this expression to be treated straightforwardly. On the other hand, if the effect of the stress were described purely through a boundary condition on the flow velocity (i.e. we formulated the same problem for flow A) this term would become a surface integral. As already mentioned, this would lead to complications due to boundary variation when variations are taken with respect to $\bar{v}_1$ to determine stationary values of $\mathscr{L}$, that can be straightforwardly avoided by considering flow B.

Throughout the derivation of the equations that must be satisfied for bounding solutions for the functional $\mathscr{L}$, we allow the shape function σ to take arbitrary form (subject to the normalization constraint $\langle \sigma^2\rangle = 1$). However, before we calculate solutions numerically, we discuss, in § 4.3, the selection of a particular form of σ for which it is possible to draw a correspondence between flows A and B. Whatever the particular choice of σ, if ϕ can be chosen so that $\mathscr{L}$ has a minimum over all possible fields $\boldsymbol{v}$, then this value of $\mathscr{L}$ must lead to a rigorous lower bound on the dissipation, as any actually realizable $\boldsymbol{u}$ that satisfies the governing equations must be accessible by some appropriate choice of $\boldsymbol{v}$. Maximizing the minimum over all ϕ and a then yields the best possible lower bound (see Kerswell 1998 for more discussion of the underlying principles).

A necessary condition for an extremum of $\mathscr{L}$ to exist is that $\mathscr{L}$ satisfies six Euler–Lagrange equations: with respect to the Lagrange multiplier a; the background field ϕ; the mean part of the streamwise fluctuation velocity $\bar{v}_1$; and the three meanless components of the fluctuation field $\hat{v}_1$, $\hat{v}_2$ and $\hat{v}_3$. Using the Euler–Lagrange equation

for variations with respect to $\bar{v}_1$, and applying the boundary conditions in (4.4), we can relate $\bar{v}_{1z}$ to ϕ_z through

$$\bar{v}_{1z} = -\phi_z + \frac{\lambda}{2}(\phi_z - G\sigma) \text{ where } \lambda \equiv \frac{a}{a+1}, \tag{4.9}$$

which together with the Euler–Lagrange equation for variations with respect to ϕ yields

$$\lambda\phi_z = (\lambda - 2)G\sigma + 2\overline{\hat{v}_1\hat{v}_3}. \tag{4.10}$$

Using (4.9) and (4.10), the remaining Euler–Lagrange equations become

$$\lambda = \langle \|\nabla\hat{\boldsymbol{v}}\|^2\rangle / G\,\langle\sigma\hat{v}_1\hat{v}_3\rangle, \tag{4.11}$$

$$2\nabla^2\hat{\boldsymbol{v}} - \lambda\phi_z \begin{pmatrix} \hat{v}_3 \\ 0 \\ \hat{v}_1 \end{pmatrix} = \nabla\hat{p}, \tag{4.12}$$

where the pressure has been rescaled by $\hat{p} = p/(a+1)$, and the meanless fluctuation velocity $\hat{\boldsymbol{v}}$ is incompressible and satisfies the homogeneous boundary conditions

$$\hat{\boldsymbol{v}} = 0 \quad \text{at } z = -1, \quad \hat{v}_{1z} = \hat{v}_{2z} = \hat{v}_3 = 0 \text{ at } z = 0. \tag{4.13}$$

Cubic terms of the form $\langle\hat{v}_1\hat{v}_3\phi_z\rangle$ and $\langle\hat{v}_1\hat{v}_3\sigma\rangle$ have been eliminated by taking the volume average of the dot product of $\hat{\boldsymbol{v}}$ and the left-hand side of (4.12) and manipulating the Euler–Lagrange equation for variations with respect to a using the momentum flux constraint

$$\overline{\hat{v}_1\hat{v}_3} - \phi_z - \bar{v}_{1z} - G\sigma = 0, \tag{4.14}$$

which can be obtained by combining (4.9) and (4.10). This constraint is clearly equivalent to $\mathscr{D}_3 = 0$ in (3.2). Expressions for the cubic terms are also useful in that using them in the volume average of the product of (4.10) and $\hat{v}_1\hat{v}_3$ eventually yields the expression

$$\langle \|\nabla\hat{\boldsymbol{v}}\|^2\rangle = a\langle(\overline{\hat{v}_1\hat{v}_3})^2\rangle, \tag{4.15}$$

and so any non-trivial solution with $\hat{\boldsymbol{v}} \neq \boldsymbol{0}$ requires $a > 0$, and hence $0 < \lambda < 1$.

Substituting (4.9) into (4.8) eventually yields

$$\mathscr{L} = G^2 - \frac{\langle[\lambda\phi_z + (2-\lambda)G\sigma]^2\rangle}{4(1-\lambda)} + \frac{\mathscr{H}}{(1-\lambda)}, \tag{4.16}$$

where $\mathscr{H}$ is the quadratic form

$$\mathscr{H}[\phi, \hat{\boldsymbol{v}}, \lambda] = \langle \|\nabla\hat{\boldsymbol{v}}\|^2\rangle + \lambda\,\langle\hat{v}_1\hat{v}_3\phi_z\rangle. \tag{4.17}$$

A stationary value of $\mathscr{L}$ is a lower bound on ε if the minimum of the quadratic form $\mathscr{H}$ exists as $\hat{\boldsymbol{v}}$ ranges over the set of incompressible vector fields which satisfy the boundary conditions in (4.13). This requires that $a > 0$ and that the spectral constraint

$$\mathscr{H}[\phi, \hat{\boldsymbol{v}}, \lambda] \geqslant 0 \tag{4.18}$$

is satisfied for all incompressible vector fields satisfying the boundary conditions in (4.13).

In this case the lower bound on the non-dimensional dissipation is thus

$$\langle \|\nabla\boldsymbol{u}\|^2\rangle \geqslant \frac{h^4}{\nu^3}\varepsilon_{\min} = G^2 - \frac{\langle[\lambda\phi_z + (2-\lambda)G\sigma]^2\rangle}{4(1-\lambda)}. \tag{4.19}$$

These expressions are superficially similar to those derived in § 3, particularly when we draw the correspondence of $a\phi_z$ and $G\theta$. However, before comparing the equations closely, we explain briefly how we identify the solutions for $\hat{\boldsymbol{v}}$, λ, and ϕ associated with the best possible lower bound on ε.

4.1. *Solution technique*

Here we apply the technique discussed in PK03. We solve the Euler–Lagrange equations (4.10)–(4.12) numerically using the method of pseudo-spectral collocation (Boyd 2001), assuming no streamwise dependence of the bounding solution (Busse 1969*a*, 1970), and hence $\partial/\partial x = 0$.

We expand the background and fluctuation fields in Chebyshev polynomials in the vertical direction to ensure adequate resolution in the expected boundary layers. Spanwise variation is expressed in Fourier modes. The calculation of the asymptotic lower bound can be separated into two steps: first we identify the energy stability point G_{ES} where the laminar solution ceases to be a global attractor (the uniqueness implies that the laminar solution is both upper and lower bound below this energy stability point). We then use the numerical continuation package PITCON (Rheinboldt & Burkhardt 1983*a*, *b*) to continue the solution of the Euler–Lagrange equations away from the laminar solution for higher G, adding further structure through spanwise-periodic subfields as required to satisfy the spectral constraint (see PK03 for further details).

4.2. *Continuation calculation from the laminar solution*

From (4.10) and (4.14), the laminar solution (where $\boldsymbol{u} = u_{\mathrm{L}}(z)\hat{\boldsymbol{\imath}}$) corresponds to $\lambda = 1$ (or equivalently $a \to \infty$), $\bar{v}_1 = 0$, and

$$\phi_{\mathrm{L}z} = u_{\mathrm{L}z} = -G\sigma, \tag{4.20}$$

which recovers the laminar dissipation ε_{L} of $\nu^3 G^2/h^4 = u_\star^4/\nu$. The spectral constraint for the laminar solution is thus

$$\mathscr{H}_{\mathrm{L}} \equiv \langle \|\boldsymbol{\nabla}\hat{\boldsymbol{v}}\|^2 \rangle - G\,\langle \sigma \hat{v}_1 \hat{v}_3 \rangle \geqslant 0, \tag{4.21}$$

for all incompressible $\hat{\boldsymbol{v}}$ satisfying the boundary conditions (4.13). The circumstances under which the laminar solution satisfies the spectral constraint (4.21) are, as in the plane Couette flow considered in PK03, linked to the energy stability of the laminar solution. It can be shown that (4.21) is equivalent to the requirement that the laminar flow is energy stable to arbitrary perturbations $\hat{\boldsymbol{v}}$, in the sense that the kinetic energy of these perturbations decays with time (see Joseph 1976).

Therefore, while the flow is energy stable, the dissipation has a lower bound given by the laminar solution, i.e. $\langle \|\boldsymbol{\nabla u}\|^2 \rangle = G^2$, irrespective of the particular structure of the body-force shape function σ. As G is increased, for any given σ, there must be a value at which the flow becomes marginally energy stable, i.e. a non-trivial velocity perturbation develops such that (4.21) is marginally satisfied. As G is increased, the laminar solution will no longer satisfy the spectral constraint (4.21), whereas the new perturbation will, and it is possible to continue this non-trivial solution (using PITCON) to higher G (and in general $\lambda < 1$) while still satisfying the set (4.10)–(4.12) and the spectral constraint (4.18) for non-trivial ϕ_z and λ. Therefore, the second term on the right-hand side of (4.19) becomes non-zero, and the lower bound on the dissipation decreases from its laminar value G^2.

4.3. *Appropriate choice of shape function σ*

As already noted, for the two flows A and B to approach equivalence, it is necessary for the body-forcing shape function σ to vary significantly only within a sufficiently thin upper boundary region. As possible appropriate choices for σ, we considered a sequence of shape functions σ of the form

$$\sigma(z) = -c_1(1 - \mathrm{e}^{c_2 z}), \quad c_1 = \sqrt{\frac{2c_2}{2c_2 - 1 + 2\mathrm{e}^{-c_2} - \mathrm{e}^{-2c_2}}}, \tag{4.22}$$

where c_1 is defined by requiring that $\langle \sigma^2 \rangle = 1$. As c_2 increases, and hence the region over which σ differs significantly from -1 becomes progressively localized in the vicinity of the upper boundary at $z = 0$, the flows driven by these body forcings approach flow A arbitrarily closely.

Indeed, for this choice of σ, as c_2 increases, we found that the critical G for energy stability converged towards $G_c = G_{ES} = 51.7$, which is naturally the energy stability point for flow A. At this critical G, the laminar spectral constraint (4.21) is marginally satisfied, and there exists some marginal incompressible eigenfunction $\hat{\boldsymbol{v}}_{ES}$ such that $\mathscr{H}_{\mathrm{L}}[\phi_{\mathrm{L}}, \hat{\boldsymbol{v}}_{ES}, 1] = 0$ and so the flow is marginally globally asymptotically stable or energy stable (Joseph 1976). The marginal eigenfunction $\hat{\boldsymbol{v}}_{ES}$ has horizontal spanwise wavenumber $l_1 = l_{ES} = 2.08$, consistently with the results presented in the Appendix. From this point we can start our continuation by adjusting the amplitude of the eigenfunction until convergence to a non-trivial solution for $G > G_{ES}$ occurs, and march on to higher G.

4.4. *The spectral constraint and incoming wavenumbers*

During the continuation process with PITCON, it is always necessary to check that the solutions to the Euler-Lagrange equations (4.10)–(4.12) actually correspond to a rigorous lower bound on dissipation, i.e. they satisfy the spectral constraint. Following PK03, enforcing $\mathscr{H}$ to be positive-semidefinite corresponds to solving a linear eigenvalue problem of the form

$$2\nabla^2 \hat{\boldsymbol{v}} - \lambda \phi_z \begin{pmatrix} \hat{v}_3 \\ 0 \\ \hat{v}_1 \end{pmatrix} - \nabla \hat{p} = \mu \hat{\boldsymbol{v}} \tag{4.23}$$

over the particular function space Ψ defined as

$$\Psi = \{\hat{\boldsymbol{v}} \mid l\hat{v}_2 + \hat{v}_3' = 0, \overline{\hat{\boldsymbol{v}}} = \boldsymbol{0}, \hat{\boldsymbol{v}}(-1) = \boldsymbol{0}, \hat{v}_{1z}(0) = \hat{v}_{2z}(0) = \hat{v}_3(0) = 0\} \tag{4.24}$$

with eigenvalues $\mu \leqslant 0$ over the real space of l, the wavenumber in the cross-stream direction. Using $\overline{\mu}(l)$ to denote the maximum of this eigenvalue problem in l, it is quite clear that $\overline{\mu}(l) = 0$ correspond to flow fields that satisfy the Euler–Lagrange equations (4.10)–(4.12). Following the continuation procedure, we find similar behaviour to that discussed in PK03. At the critical G when $G_{ES} = 51.7$, a unique $l_1 = l_{ES}$ exists such that $\overline{\mu}(l_{ES}) = 0$. This wavenumber l_1 satisfying $\overline{\mu} = 0$ varies with the continuation of G, and at a certain point another local maximum develops in $\mu(l)$ (see PK03 figure 1 for a clear demonstration of a new local maximum emerging). We extend the solution as PK03 previously did to include more fluctuation subfields every time this behaviour happens, and so we can identify the bifurcation structure of the bounding solution as G increases.

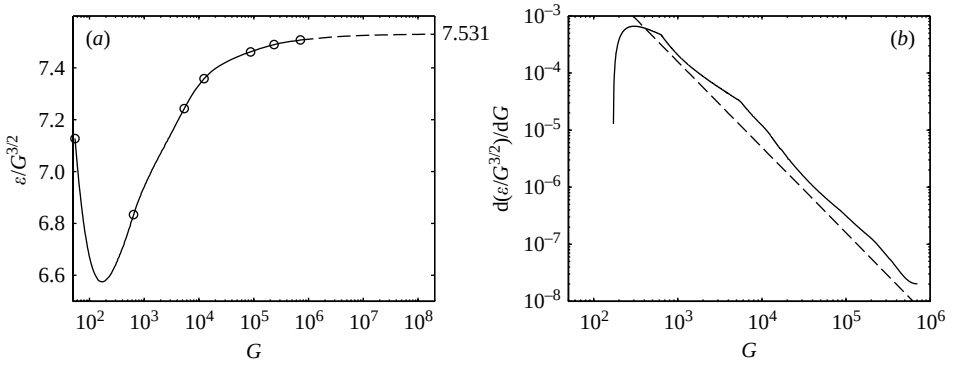

FIGURE 3. (*a*) Variation of the lower bound on the scaled long-time averaged dissipation rate γ as defined in (3.15) with G. The predicted asymptotic value at high G is marked with a dashed line. The bifurcation points at which new spanwise wavenumbers enter the solution are marked with circles. (*b*) $d\gamma/dG$ against G (where γ is as defined in (3.15)), showing that $d\gamma/dG = O(G^{-3/2})$ as $G \to \infty$ (the dashed line is a plot of $G^{-3/2}$).

4.5. *Results*

We have solved (4.10), (4.11), and (4.12) subject to the boundary conditions (4.13) and the spectral constraint (4.18). We have calculated to the 7th bifurcation ($G = 7.06 \times 10^5$), with certain asymptotic behaviours being observed. The most important asymptotic behaviour is the scaling of the lower bound of the dissipation rate ε_{min} as defined in (4.19). To ensure accurate comparison between the results for the surface-stress-driven flow A and the body-force-driven flow B, we chose σ to take the form (4.22) with sufficiently large c_2 so that, to the finite resolution of our vertical representation in terms of Chebyshev polynomials, the shape function σ is indistinguishable from the discontinuous profile

$$\sigma(z) = 0, \quad z \neq 0, \quad \sigma = 0, \quad z = 0. \tag{4.25}$$

This essentially entailed increases in c_2 whenever more Chebyshev polynomials were required to be added to ensure adequate vertical resolution for the boundary layers associated with the bounding solutions.

As we have discussed in § 2, the upper bound $\varepsilon_{max} = \nu^3 G^2/h^4 = u_\star^4/\nu = \varepsilon_L$, and from the continuation calculation we can see in figure 3(*a*) that the lower bound $h^4\varepsilon_{min}/\nu^3 = O(G^{3/2})$ as $G \to \infty$, confirming that the simple bound developed in § 3 still captures the correct asymptotic scaling. This is due to an exact cancellation of G^2 in our functional $\mathscr{L}$, which we discuss in more detail below. The lower bound decreases from G^2 at the energy stability point and develops a local minimum at $G = 170.067$, where the scaled dissipation γ, defined in (3.15), is bounded by

$$\gamma = \Gamma G^{1/2} = \frac{h^4\varepsilon}{\nu^3 G^{3/2}} = \frac{h\varepsilon}{u_\star^3} \geqslant 6.5751. \tag{4.26}$$

The lower bound then increases with G, and gradually approaches an asymptotic value.

Indeed the largest value of G that we are able to consider is constrained by round-off error, due to the sensitivity of the spectral constraint. In the plateau region of the $\overline{\mu}(l)$ graph at $G = 7.06 \times 10^5$, where a new spanwise mode is about to emerge, $\overline{\mu} = O(10^{-6})$ and $\hat{v}_{new} = O(1)$, whereas the largest term on the left-hand side of (4.23) is $O(10^8)$ near the surface $z = 0$. As discussed in PK03, this huge difference in orders

tests the capability of double precision, and made it impossible to identify the narrow region of convergence for the next bifurcation. At this stage, $\gamma \geqslant 7.507$. However, the bound on γ has clearly not yet converged to an asymptotic value. This lack of convergence can be explained by appreciating that lower-order (in terms of powers of $G^{1/2}$) contributions to the bound are still significant. Indeed, since as shown in figure 3(*b*) $\mathrm{d}\gamma/\mathrm{d}G = O(G^{-3/2})$, the data suggest that $\gamma \geqslant 7.531 - 20.3G^{-1/2}$ is a more appropriate form for the lower bound.

Considering the dimensional dissipation ε, as already noted this asymptotic scaling implies that $\varepsilon = O\left(u_\star^3/h\right)$ as $G \to \infty$, and so the best possible bound on the mechanical energy dissipation rate is independent of the kinematic viscosity ν, which is to be expected at high G, and is consistent with the results presented in § 3. Although not reported here, the bifurcation structure is similar to that discussed in detail in PK03.

Therefore, it is apparent that the best possible bound on dissipation rate generated using the CDH method (i.e. $\gamma G^{1/2} = \Gamma \geqslant 7.531G^{-1/2} - 20.3G^{-1}$) exhibits the same leading-order scaling as that generated by using the family of trial functions θ defined in (3.10) (i.e. $\Gamma \geqslant 4.785G^{-1/2}$). Not unexpectedly, the trial function approach under-estimates the best possible coefficient for the leading-order scaling by 35%. The reasons for this under-estimation can be better understood if we have a detailed understanding of the properties of the best possible bounding solutions to the problem formulated using the CDH method.

4.6. *Detailed discussion of the CDH bounding solution*

The most important defining aspects of the bounding solution are shown in figure 4. Figure 4(*a*) shows how the parameter λ, defined in (4.9), varies with G. Subsequently to the energy stability point (where $\lambda = 1$) there is a relatively narrow range of G in which λ decreases with an $O(G^{-1})$ dependence. However as $G \to \infty$, $\lambda \to 3.76G^{-1/2}$. Figure 4(*b*) shows that the flow develops boundary layers at both the top and bottom. Both boundary layers have thicknesses of $O(G^{-1/2})$ as $G \to \infty$, though the particular selection of this scaling factor is somewhat arbitrary, as it depends on our choice of the definition of an appropriate edge of the boundary layer.

For the lower boundary layer, we define its edge as the location where the gradient ϕ_z has dropped to 2.5% of its maximum (boundary) value. Since ϕ_z is by definition zero at the upper boundary, we are unable to use exactly the same definition. However, near the upper boundary, as is apparent in figure 4(*c*), where $a\phi_z$ is plotted against z for $G = 12102$, ϕ_z drops to negative values before reverting towards zero in the interior of the flow. (Somewhat similarly to the situation discussed in § 3, the structure of ϕ_z, acting as it does to impose the horizontally averaged streamwise momentum constraint, as is apparent in (4.7), tends towards being zero in the interior of the flow, where this constraint does not play a strong role.) Therefore, we define the edge of the upper boundary layer as being located at the place where ϕ_z reaches its local minimum value. The existence (or not) of an upper boundary layer is a qualitative difference between the solutions associated with the two bounds, and is likely to be significant in the under-estimation of the best possible bound by using the family of functions $\theta(z)$ as defined in § 3.2. We discuss the differences in more detail below in § 4.7. Also on figure 4(*c*), we plot $G\theta(z)$ at $G = 12102$ (where the appropriate value of m is $m = 5$) that corresponds to the lower bound on the mechanical energy dissipation rate calculated in § 3, showing clearly that the two profiles are similar, except in the upper boundary layer.

Furthermore, the existence of an identifiable upper boundary layer in the bounding solution imposes an obvious constraint on the required structure of the shape function

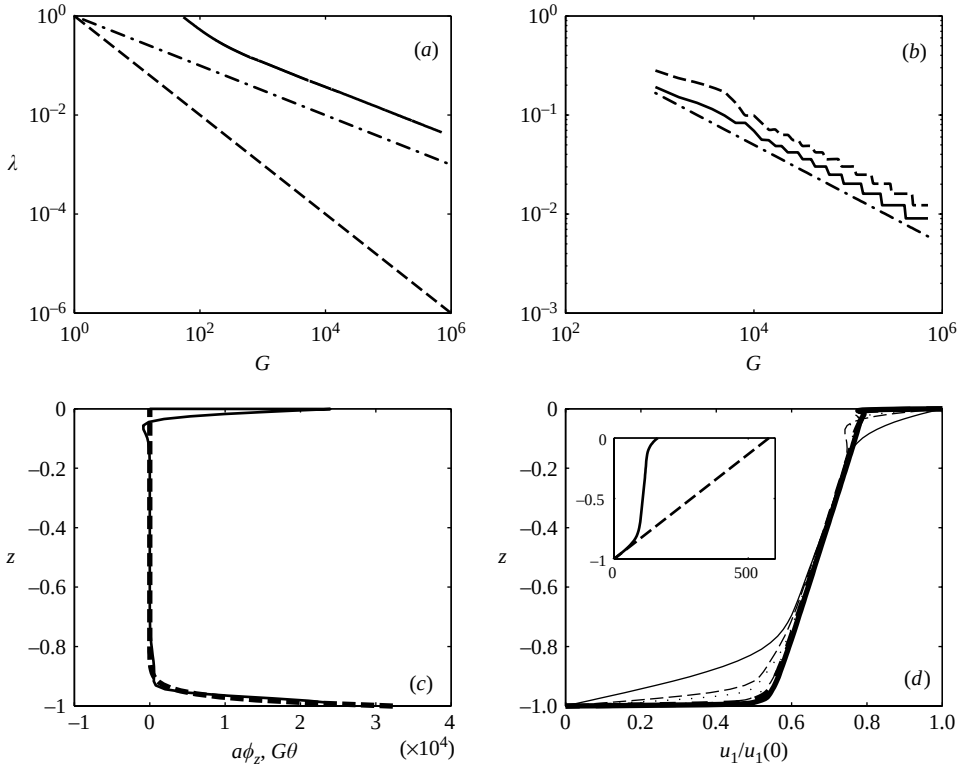

FIGURE 4. (*a*) The parameter λ (as defined in (4.9)) against G. The dashed line is G^{-1} and the dash-dotted line is $G^{-1/2}$. (*b*) The upper boundary layer thickness against G, (shown with a solid line, and defined by the distance between the boundary and the location of the minimum in ϕ_z) and the lower boundary layer thickness against G (dashed line, and defined by the distance between the lower boundary and the location where ϕ_z drops to 2.5% of its boundary value). The dash-dotted line is proportional to $G^{-1/2}$. The staircase structure is due to the finite spectral representation in terms of Chebyshev polynomials. (*c*) Comparison of the vertical structure of the Lagrange multiplier $a\phi_z$ for the horizontally averaged streamwise momentum for the bounding solutions generated by the CDH method (plotted with a solid line) and the equivalent Lagrange multiplier $G\theta$ (plotted with a dashed line) for bounding solutions generated in § 3 when $G = 12102$. (*d*) The horizontally averaged streamwise velocity $\bar{u}_1$ normalized by $\bar{u}_1(0)$ at various values of G: 576.8 (thin solid line); 5185 (dashed line); 12102 (dotted line); 87338 (dot-dashed line); 234360 (thick solid line). In the inset we compare the unscaled mean velocity profile associated with the lower bound on the mechanical energy dissipation rate (solid line) with the laminar velocity profile (dashed line) at $G = 576.8$.

σ for correspondence to be possible between flow A and flow B. For the localized variation of σ near the upper boundary to be an appropriate model for surface-stress forcing, the region of variation of σ must clearly be embedded within the upper boundary layer of the velocity fields associated with the bounding solutions.

The effect of these various scaling relationships on the calculated bound can be understood by consideration of stationary values of the functional $\mathscr{L}$ (as defined in (4.16) corresponding to circumstances when $\mathscr{H} = 0$). As $G \to \infty$, since $\langle \sigma^2 \rangle = 1$, there is an exact cancellation in the $O(G^2)$ terms, and so

$$\mathscr{L} \approx -\frac{\lambda^2 \langle \phi_z^2 \rangle}{4} - \lambda G \langle \sigma \phi_z \rangle. \tag{4.27}$$

Balance in (4.10) near the boundaries implies that $\phi_z = O(G^{3/2})$ in the boundary layers. Since, as shown in figure 4, the boundary layer thickness is proportional to $G^{-1/2}$ at high G, $\langle \phi_z \rangle = \phi(0) = O(G)$, while $\langle \phi_z^2 \rangle = O(G^{5/2})$. From (4.27), it is clear that both $\lambda^2 \langle \phi_z^2 \rangle$ and $\lambda G \langle \sigma \phi_z \rangle$ are of $O(G^{3/2})$, exactly the same scaling we have found in our solution for $\mathscr{L}$. Since $a > 0$, and so $\lambda > 0$, equation (4.10) implies that ϕ_z has the opposite sign to σ, and so $-\lambda G \langle \sigma \phi_z \rangle$ is positive. Furthermore, since $\sigma \approx -1$ over virtually all the depth of the layer, $-\langle \sigma \phi_z \rangle \approx \langle \phi_z \rangle = O(G^{3/2})$. It is therefore apparent that the expression (4.27) contains two $O(G^{3/2})$ terms, one positive and one negative.

These results also allow us to interpret the properties of the mean profile, as plotted in figure 4(*d*). Using (4.9) and (4.10),

$$\bar{u}_{1z} = \frac{\lambda}{2} [\phi_z - G\sigma] = -G\sigma + \overline{\hat{v}_1 \hat{v}_3}. \tag{4.28}$$

These expressions have several important implications, which help to explain why the lower bound on the dissipation is so much less than the laminar solution (particularly at higher values of G) as is apparent in the inset of figure 4(*d*). Near the upper and lower boundary, since $\phi_z = O(G^{3/2})$ and $\lambda = O(G^{-1/2})$, $u_z = O(G)$, the same order of gradient as the laminar solution. Indeed, provided the region over which σ varies is embedded within the boundary layer of the bounding solutions (i.e. where $\overline{\hat{v}_1 \hat{v}_3} \to 0$), $u_z \approx G$ in the immediate vicinities of the two boundaries. Therefore, the mean profile has the same strong gradient G in narrow boundary layers, of depth $O(G^{-1/2})$, as the laminar solution. On the other hand, throughout the interior of the flow, since $\overline{\hat{v}_1 \hat{v}_3} \ll 0$ and hence $\phi_z \approx 0$, $\bar{u}_1$ has a weak shear of $-\lambda G\sigma/2 = O(G^{1/2})$, as is also clear in the inset figure.

Interestingly, the bounding profile $\bar{u}_1(z)$ is qualitatively similar in structure to that predicted to maximize the long-time average of the dissipation in plane Couette flow (see PK03). The pair of strong boundary layers with a significantly weaker interior shear may therefore be a generic characteristic of solutions associated with bounding the dissipation in general shear flow problems. It is also important to remember that, as noted by PK03, the boundary layers that are predicted by the CDH method do not exhibit the characteristic log-layer structure of high-Reynolds-number wall-bounded flows. This discrepancy raises the issue of how physically realistic the bounding profiles $\bar{u}_1(z)$ are, an issue we return to in the next section.

Also, from (4.28), it is apparent that

$$\overline{u}(0) = \frac{\lambda}{2} [\phi|_{z=0} - G\langle \sigma \rangle], \tag{4.29}$$

which is $O(G^{1/2})$. Therefore, at larger values of G, there is once again substantial deceleration of the surface horizontally averaged streamwise velocity for the lower bounding solutions by comparison with the laminar solution. Indeed, just as we observed in § 3, the dimensional surface mean velocity is $\bar{u}_1(0) \propto (\tau/\rho)^{1/2} = u_\star$, which is independent of viscosity. As we noted above, this is entirely reasonable, since, when G is large, we expect physically that the viscosity ν is unimportant, and so the flow is driven by the friction velocity $u_\star$. This characteristic, shared by the two bounds, appears to be fundamental to the determination of the $O(u_\star^3/h)$ scaling for the mechanical energy dissipation rate.

4.7. *Comparison of the properties of the two bounds*

From an understanding of the various properties of the two bounds which we have constructed, it is apparent why the bound constructed in § 3 under-estimates

quantitatively the bound constructed numerically using the CDH method. Fundamentally, this occurs because, unlike in the CDH method, the Lagrange multiplier θ cannot be used formally to construct the horizontally averaged velocity field associated with the bounding solution. Therefore, there is no way to calculate the contribution from the second to last term $\langle[\bar{u}_{1z} + G(\alpha - \theta)/2]^2\rangle$ on the right-hand side of (3.4), which inevitably will lead to a non-zero contribution to the value of the dissipation ε. Indeed, in general, non-zero values of this term will imply that the value of the parameter α given in (3.8) that leads to (3.9) actually does not correspond to the best possible value of α to minimize ε.

On the other hand, since the CDH method allows direct determination of all aspects of the velocity fields associated with the bounding solution, we are able to analyse the significance and structure of the (meanless) fluctuations associated with the bounding solution. In particular, as G increases, more and more fluctuation subfields must be included in the solution to ensure that the spectral constraint remains satisfied. We find that these subfields have a clear self-similar structure consistent with previous work (see PK03 for a more detailed discussion).

Furthermore, as already noted, since the function $\theta(z)$ is restricted to belong to a restricted family defined by (3.10), the bound considered in § 3 does not allow for the presence of an upper boundary layer in the Lagrange multiplier, a naturally developing characteristic of the bound generated by the CDH method. It is reasonable to suppose that such a discrepancy will lead inevitably to a quantitative difference between the two bounds. Indeed, the close (yet not perfect) agreement between $G\theta$ and $a\phi_z$ over much of the flow depth (as shown in figure 4*c*) suggests yet another subtle, yet possibly important, reason why the bound generated in § 3 is not as good as possible. If we identify $G\theta$ with $a\phi_z$ the constraint $\mathscr{J} \geqslant 0$ as defined in (3.5) for the bounding solution constructed in § 3 is actually stronger than the spectral constraint $\mathscr{H} \geqslant 0$ defined in (4.18). Since $\lambda < a$, a particular marginal choice of ϕ_z, or equivalently θ with $\mathscr{H} = 0$, will be acceptable within the CDH problem formulation, yet will not be an acceptable choice as a trial function since $\mathscr{J} < 0$.

5. Conclusions

This paper presents a complete solution to the CDH problem for the rigorous lower bound on dissipation in surface-stress-driven flow up to the seventh spanwise wavenumber bifurcation which occurs at $G = 7.06 \times 10^5$. The asymptotic value of the lower bound can be predicted to be $\langle\|\boldsymbol{\nabla u}\|^2\rangle \geqslant 7.531G^{3/2} - 20.3G$, i.e. $\varepsilon \geqslant 7.531u_\star^3/h - 20.3u_\star^2\nu/h^2$ where $u_\star$ is the friction velocity defined by $\tau = \rho u_\star^2$ and τ is the (upper) surface stress. We show how the leading-order scaling arises naturally from a straightforward calculation imposing the natural constraints of total power balance and horizontally averaged streamwise momentum balance, although the particular quantitative scaling factor is somewhat underestimated. That underestimation occurs largely because of strong simplifying assumptions made during the solution of the required optimization problem, as discussed above in § 4.7.

Our choice of an equivalent body-forced flow problem B (with body forcing restricted to a sufficiently narrow region in the vicinity of the upper boundary) to model the surface-stress-driven flow (referred to throughout this paper as flow A) also allows us to draw comparisons with previous work on body-forced flow. For example, Doering & Foias (2002) and Doering *et al.* (2003) found for body-forced turbulence that variational bounds on the non-dimensional mechanical energy dissipation rate should take the form $c_1Re^3 + c_2Re^2$, where c_1 and c_2 depend in some

way upon the particular structure of the body force, and the Reynolds number has been appropriately defined in terms of the velocity and length scales of the forcing. In our flow, from the definition of G in (2.6), G can be identified with a square of a friction Reynolds number Re_f defined in terms of a friction velocity $u_\star$, i.e. $G^{1/2} = Re_f \equiv u_\star h/\nu$, and so the lower bound scaling $\gamma \geqslant 7.531 - 20.3G^{-1/2}$ (with γ defined as in (3.15)) is consistent with the results of Doering and co-workers, with $c_1 = 7.531$ and $c_2 = -20.3$ in their formulation.

However, as is always the case with analyses of this kind, the lower bound that we have determined must be treated with caution. Although it seems quite plausible that at high G the mechanical energy dissipation rate should be independent of the flow viscosity (and so, dimensionally $\varepsilon = O(u_\star^3/h)$, a scaling consistent with our calculations) there is no rigorous reason why a stationary flow should be organized so as to minimize its mechanical energy dissipation rate. Secondly, even if the scaling is correct, there is no reason to suppose that the quantitative numerical factors which we have determined yield a 'tight' bound, in the sense that there actually exists a realizable flow that has an associated dissipation which approaches closely the predicted lower bound. Indeed, since we only impose two integral constraints consistent with, but substantially weaker than, the incompressible Navier–Stokes equations, we optimize over a class of vector fields that constitute a superset of the solutions to the true governing equations. Therefore, it is unclear whether the constructed bound is attainable by flows that satisfy the Navier–Stokes equations.

Indeed, there are cogent reasons to suppose that real flows are unlikely to replicate the predicted mean velocity profile of the bounding solution generated by the CDH method. As noted by PK03 for the plane Couette flow, the boundary layers predicted by the bounding solution do not exhibit the log-layer character that is typical of wall-bounded flows. Furthermore, it is not established whether the predicted profile can be sustained over a sufficiently long time to be consistent with the modelling assumptions. The natural way to address these issues is through numerical simulation (as done recently for the related problem of body-forced plane shear flow with stress-free boundary conditions by Doering *et al.* 2003). We intend to report in due course the results of such simulations of both flows A and B to adequately high Gr to identify the asymptotic scaling behaviour. Using such simulations, we will be able to calculate directly the actual long-time average of the mechanical energy dissipation rate, as well as the associated mean flow structures, which we can then compare with the bounding solutions presented here.

We would like to thank Richard Kerswell for many useful discussions, and Stephen Plasting for allowing us to use and modify his numerical code. This work was supported by the National Science Foundation under the Collaborations in Mathematical Geosciences (CMG) initiative (ATM-0222104).

Appendix. Critical flows and the energy stability condition

To obtain the strongest possible bound in § 3 we adjust the amplitude of the function $\theta(z)$ in (3.5), say $\beta \equiv \langle\theta\rangle$, so that $\theta(z)$ is *critical*. This means that there is a special $\boldsymbol{v} = (v_1, v_2, v_3)$, say $\boldsymbol{v}_*$, for which

$$\mathscr{J}[\boldsymbol{v}_*; \theta] = 0. \tag{A 1}$$

The functional $\mathscr{J}[\boldsymbol{v}, \theta] \equiv \langle \|\boldsymbol{\nabla v}\|^2 \rangle + G\langle \theta v_1 v_3 \rangle$ is positive for all other v. Well-known arguments show that $\theta(z) = \beta\hat{\theta}(z)$ is critical provided that the following linear problem

m	βG	l
0	51.73	2.08
1	66.72	2.22
2	91.28	2.52
3	122.74	3.00
4	157.95	3.56
5	195.09	4.20
10	388.16	8.08

TABLE 1. Solutions of the eigenproblem (A 2) with the exponential profile from (3.10).

has a non-trivial solution:

$$-2\nabla^2 \boldsymbol{v}_* + \beta G \begin{pmatrix} \hat{v}_{*3} \\ 0 \\ \hat{v}_{*1} \end{pmatrix} \hat{\theta}(z) = -\nabla p. \tag{A 2}$$

This eigenproblem determines the eigenvalue, βG, as a *functional* of the profile $\hat{\theta}(z)$.

To solve (A 2) we assume that $\boldsymbol{v}_*$ is independent of x and takes the form of spanwise rolls. Thus the eigensolution has the form

$$v_{*1}(y, z) = -2\mathrm{i}\mathrm{e}^{\mathrm{i}ly}\chi(z) + \text{c.c.}, \tag{A 3}$$

$$\Psi(y, z) = \mathrm{e}^{\mathrm{i}ly}\psi(z) + \text{c.c.}, \tag{A 4}$$

where the spanwise circulation is

$$(v_{*2}, v_{*3}) = (-\Psi_z, \Psi_y). \tag{A 5}$$

The functions χ and ψ are both real. Substituting into (A 2) leads to a sixth-order boundary value problem which is solved using the spectral methods of Weideman & Reddy (2000). Thus, to construct a critical $\theta(z)$ we pick a normalized profile $\hat{\theta}(z)$ and then find the amplitude β by locating the smallest eigenvalue of (A 2). Some results for the exponential profile in (3.10) are summarized in table 1.

REFERENCES

BOYD, J. P. 2001 *Chebyshev and Fourier Spectral Methods*, 2nd edn. Dover.

BUSSE, F. H. 1969*a* Bounds on the transport of mass and momentum by turbulent flow. *Z. Angew. Math. Phys.* **20**, 1–14.

BUSSE, F. H. 1969*b* On Howard's upper bound for heat transport by turbulent convection. *J. Fluid Mech.* **37**, 457–477.

BUSSE, F. H. 1970 Bounds for turbulent shear flow. *J. Fluid Mech.* **41**, 219–240.

BUSSE, F. H. 1978 The optimum theory of turbulence. *Adv. Appl. Mech.* **18**, 77–121.

CHILDRESS, S., KERSWELL, R. R. & GILBERT, A. D. 2001 Bounds on dissipation for Navier-Stokes flow with Kolmogorov forcing. *Physica* D **158**, 105–128.

CONSTANTIN, P. & DOERING, C. R. 1995 Variational bounds on energy dissipation in incompressible flows: II. Channel flow. *Phys. Rev.* E **51**, 3192–3198.

COURANT, R. & HILBERT, D. 1953 *Methods of Mathematical Physics, Volume 1*, 1st English edn. Interscience.

DOERING, C. R. & CONSTANTIN, P. 1992 Energy dissipation in shear driven turbulence. *Phys. Rev. Lett.* **69**, 1648–1651.

DOERING, C. R. & CONSTANTIN, P. 1994 Variational bounds on energy dissipation in incompressible flows: Shear flow. *Phys. Rev.* E **49**, 4087–4099.

Doering, C. R. & Constantin, P. 1996 Variational bounds on energy dissipation in incompressible flows: III. Convection. *Phys. Rev.* E **53**, 5957–5981.

Doering, C. R., Eckhardt, B. & Schumacher, J. 2003 Energy dissipation in body-forced plane shear flow. *J. Fluid Mech.* **494**, 275–284.

Doering, C. R. & Foias, C. 2002 Energy dissipation in body-forced turbulence. *J. Fluid Mech.* **467**, 289–306.

Hopf, E. 1941 Ein allgemeiner endlichkeitssatz der hydrodynamik. *Mathematische Annalen* **117**, 764–775.

Howard, L. N. 1963 Heat transport by turbulent convection. *J. Fluid Mech.* **17**, 405–432.

Howard, L. N. 1972 Bounds on flow quantities. *Annu. Rev. Fluid Mech.* **4**, 473–494.

Howard, L. N. 1990 Limits on the transport of heat and momentum by turbulent convection with large scale flow. *Stud. Appl. Maths* **83**, 273–285.

Joseph, D. D. 1976 *Stability of Fluid Motions I.* Springer.

Kerswell, R. R. 1997 Variational bounds on shear-driven turbulence and turbulent Boussinesq convection. *Physica* D **100**, 355–376.

Kerswell, R. R. 1998 Unification of variational principles for turbulent shear flows: the background method of Doering-Constantin and the mean-fluctuation formulation of Howard-Busse. *Physica* D **121**, 175–192.

Kerswell, R. R. 2001 New results in the variational approach to turbulent Boussinesq convection. *Phys. Fluids* **13**, 192–209.

Malkus, W. V. R. 1954 The heat transport and spectrum of thermal turbulence. *Proc. R. Soc. Lond.* **225**, 196–212.

Malkus, W. V. R. 1956 Outline of a theory of turbulent shear flow. *J. Fluid Mech.* **1**, 521–539.

Nicodemus, R., Grossmann, S. & Holthaus, M. 1997*a* Improved variational principle for bounds on energy dissipation in turbulent shear flow. *Physica* D **101**, 178–190.

Nicodemus, R., Grossmann, S. & Holthaus, M. 1997*b* Variational bound on energy dissipation in plane Couette flow. *Phys. Rev.* E **56**, 6774–6786.

Nicodemus, R., Grossmann, S. & Holthaus, M. 1998*a* The background flow method. Part 1. Constructive approach to bounds on energy dissipation. *J. Fluid Mech.* **363**, 281–300.

Nicodemus, R., Grossmann, S. & Holthaus, M. 1998*b* The background flow method. Part 2. Asymptotic theory of dissipation bounds. *J. Fluid Mech.* **363**, 301–323.

Otero, J., Wittenberg, R. F., Worthing, R. A. & Doering, C. R. 2002 Bounds on Rayleigh-Bérnard convection with an imposed heat flux. *J. Fluid Mech.* **473**, 191–199.

Plasting, S. C. & Kerswell, R. R. 2003 Improved upper bound on the energy dissipation rate in plane Couette flow: The full solution to Busse's problem and the Constantin-Doering-Hopf problem with one-dimensional background field. *J. Fluid Mech.* **477**, 363–379 (herein referred to as PK03).

Rheinboldt, W. C. & Burkhardt, J. V. 1983*a* ALGORITHM 596 a program for a locally parameterized continuation process. *ACM Trans. Math. Software* **9**, 236–241.

Rheinboldt, W. C. & Burkhardt, J. V. 1983*b* A locally parameterized continuation process. *ACM Trans. Math. Software* **9**, 215–235.

Weideman, J. A. C. & Reddy, S. C. 2000 A MATLAB differentiation suite. *ACM Trans. Math. Software* **26**, 465–519.